Available on CMS information server

CMS NOTE 2006/010

The Compact Muon Solenoid Experiment

CMS Note

Mailing address: CMS CERN, CH-1211 GENEVA 23, Switzerland

24 January 2006

Muon Identification in CMS

E. James[a)]

Fermi National Accelerator Laboratory, USA

Y. Maravin[b)]

Department of Physics, Kansas State University, USA

M. Mulders[c)]

CERN, Switzerland

N. Neumeister[d)]

Department of Physics, Purdue University, USA

Abstract

We present and discuss the design, implementation, and performance of a muon identification software package in ORCA [1]. The identification algorithm accepts reconstructed tracks from the inner tracker and attempts to quantify the muon compatibility for each track using associated calorimeter and muon detector hit information. The software was designed for use in offline analysis and tries to identify muons with high efficiency while maintaining a low probability of misidentification. The muon identification algorithm is complementary by design to the standard global muon reconstruction algorithm that is seeded from stand-alone track reconstruction in the muon detectors. The performance of the algorithm based on its application to several simulated event samples is also presented.

---

a) jameseb@fnal.gov

b) maravin@phys.ksu.edu

c) Martijn.Mulders@cern.ch

d) neumeist@purdue.edu

1 Introduction

Muons with high transverse momenta are one of the probes for discovery of new phenomena as well as for precision measurements in high-energy physics. As such, the reconstruction and identification of muons is of utmost importance. The CMS detector has a robust and redundant muon system [2] to reconstruct and identify such particles. Standard muon reconstruction [3] works from outside-in, constructing stand-alone tracks in the muon detectors based on hits in the chambers and then combining them with reconstructed tracks in the silicon tracker [4]. Muon identification provides an additional tool for selecting muon candidates using an inside-out algorithm that is by design complementary to the standard muon reconstruction. The algorithm starts with all reconstructed tracks from the silicon inner tracking detector and attempts to quantify a muon compatibility for each (including those tracks with no matching stand-alone tracks in the muon detectors). Muon identification also takes advantage of information from other detector systems not used in the standard reconstruction such as associated calorimeter energy deposits in determining the compatibility of a given track with the muon hypothesis. In addition, the algorithm is able to make use of hit information from individual layers of the muon detectors, even in cases where those hits are not associated with reconstructed, stand-alone muon tracks. Lower p_{T} muons, for example, that range out within the iron yoke before depositing hits in the outer muon detector layers are difficult to reconstruct using stand-alone muon reconstruction. However, this class of muons can potentially still be identified offline via this algorithm by matching the hits found in the inner muon detector layers with reconstructed silicon tracks and examining the associated calorimeter energy deposits to see if they are compatible with those from a minimum-ionizing particle.

The muon identification algorithm is useful for physics analyses involving event signatures that contain multiple muons (e.g. $H \rightarrow ZZ^{*} \rightarrow \mu\mu\mu\mu$), where the reconstruction conditions can be relaxed for some muons. If the muon identification algorithm is used to identify one or more of the muons in these channels rather than requiring all muons to be fully reconstructed, the overall selection efficiency for these events will be increased. The muon identification algorithm can be particularly useful in cases where one has a very soft p_{T} spectrum for the lowest-energy muon in the event since these muons are more likely to range out in the detector and not be fully reconstructed. Even for event topologies in which all of the final state muons are fully reconstructed, the information provided by the identification algorithm will be useful for helping to understand muon fake rates and solving potential ambiguities at the analysis level. In addition, the algorithm will be very useful during commissioning for selecting a class of potential, unreconstructed muon candidates for studying and improving the reconstruction software.

2 Detector

2.1 Muon System

The CMS design is based on the choice of a 4 T magnetic field, obtained using a large superconducting solenoid that surrounds a silicon inner tracker, a crystal electromagnetic calorimeter, and a sampling hadron calorimeter. The magnetic field allows for precision tracking in the silicon detector and reduces the pile-up from soft hadrons in the four-station muon system located just outside the solenoid within the iron return yoke.

Three types of gaseous detectors are used to identify and measure muons [2]. The choice of the detector technologies has been driven by the very large surface to be covered and the different radiation environments. In the barrel region ($|\eta| < 1.2$), where the neutron induced background is negligible and both the muon rate and residual magnetic field are low, Drift Tube (DT) chambers are used. In the two endcaps, where the muon rate and magnetic field strength are higher and the neutron background is more significant, Cathode Strip Chambers (CSC) are utilized to extend coverage up to $|\eta| < 2.4$. Finally, Resistive Plate Chambers (RPC) are used in both regions, up to $|\eta| < 2.1$, primarily to provide high-precision timing information for use in the trigger hardware.

The layout of one quarter of the CMS muon system is shown in Fig. 1. In the barrel region, four stations of detectors are arranged in cylinders interleaved within the iron yoke. Each muon station consists of a DT and a RPC, and an additional RPC layer is incorporated in each of the first two stations to improve the trigger efficiency for low p_T muons. The segmentation along the beam direction follows the five wheels of the yoke. In each of the endcaps, the CSC and RPC chambers are located on four disks perpendicular to the beam in concentric rings around the disks, three on the disk closest to the interaction region and two on the others. The outer ring on the disk furthest from the interaction point is not part of the baseline detector design but can be included as a future upgrade. Each CSC chamber consists of six cathode strip and anode wire planes and therefore measures six independent pairs of coordinates for each muon track.

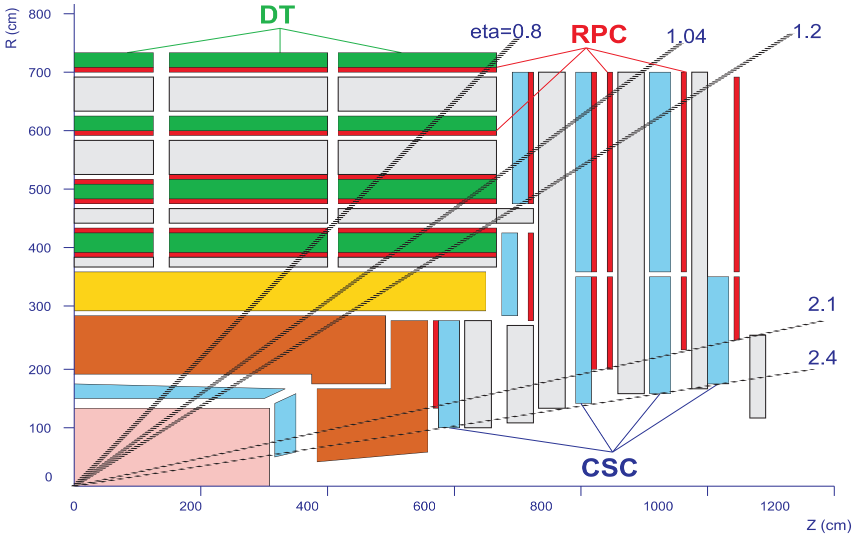

Figure 1: Layout of the CMS muon system

2.2 Calorimeters

The CMS calorimeter system consists of both electromagnetic [5] and hadronic [6] components. Muons are minimum ionizing particles (MIPs) and leave corresponding energy deposits in each section of the calorimeter along their trajectory. A typical beam-produced muon passes through the electromagnetic (ECAL), the hadronic (HCAL), and the outer hadronic (HO) sections of the calorimeter. Figure 2 shows the location of the various calorimeter detector components described in greater detail below.

The electromagnetic calorimeter (ECAL) is a hermetic, homogeneous calorimeter comprising 61200 lead tungstate ($PbWO_4$) crystals mounted in the central barrel module and 7324 crystals in each of the two endcap modules. The barrel section (EB) has an inner radius of 129 cm. It is structured as thirty-six identical super-modules, each of which covers half of the total barrel length corresponding to the the pseudorapidity interval $0 < |\eta| < 1.479$. The crystals are quasi-projective (the axes are tilted at 3° with respect to the line from the nominal vertex position) and have a front face cross section of $\sim 22 \times 22$ mm^2 and a length of 230 mm, corresponding to 25.8 X_0. The endcaps (EE) at a distance of 314 cm from the vertex cover the pseudorapidity range of $1.479 < |\eta| < 3.0$. The endcap crystals have a front face cross section of 28.6×28.6 mm^2 and a length of 220 mm, corresponding to 24.7 X_0. The high granularity of the crystals limits the effect of pileup contributions to the energy measurement [5]. A single tower as defined by the HCAL (see below) consists of an array of 5×5 crystals. Muon energy deposits are expected to be well contained within individual crystals in contrast to those associated with ionizing particles that typically produce showers over several crystals. The ECAL is situated within the 4 T solenoidal field just inside of the central hadronic calorimeter (HCAL) and has a total thickness of 1.1λ.

The hadronic calorimeter HCAL [6] is made up of four separate detector units. The barrel detector (HB) covers the central part of the detector ($|\eta| < 1.4$), and the endcap detectors (HE) cover the pseudorapidity range $1.30 < |\eta| < 3.0$. The forward calorimeters (HF) extend into the even more forward region outside the coverage of the muon detectors ($3.0 < |\eta| < 5.0$). An additional layer of scintillators, referred to as the hadron outer (HO) detector, is located outside the magnetic coil immediately in front of the first muon station. Brass has been chosen as absorber material for the hadronic calorimeter because it is non-magnetic, easy to machine, and has a reasonably short interaction length. In order to maximize the amount of absorber before the magnet, tile/fiber technology consisting plastic scintillator tiles read out with embedded wavelength-shifting (WLS) fibers has been utilized.

The barrel (HB) part of HCAL consists of 32 towers covering the pseudorapidity region $-1.4 < \eta < 1.4$ with a 5° ϕ segmentation resulting in a total of 2304 towers with a segmentation (η, ϕ) = (0.087, 0.087). The HB is constructed in two half barrels [6] and has only one longitudinal sampling. Each tower contains seventeen 5 cm thick brass plates plus two external steel plates for mechanical strength. Each endcap (HE) module of the HCAL consists of 14 towers with 5° segmentation covering the pseudorapidity region $1.3 < |\eta| < 3.0$. For the five outermost towers (at low η) the ϕ segmentation is 5° and the η segmentation is 0.087. For the eight innermost towers the ϕ segmentation is 10° while the η segmentation varies from 0.09 to 0.35 at the highest η. The total number of HE towers is 2304. The size of the HCAL calorimeter towers in the pseudorapidity region $|\eta| < 1.74$

is 0.087×0.087 in $\Delta\eta \times \Delta\phi$. In the more forward region, the size of towers in $\Delta\eta$ gradually increases reaching 0.150 around $|\eta| \sim 2.65$.

The HO layer is physically located inside the barrel muon system. It consists of scintillators embedded in the five rings of the barrel return yoke. The dimensions of the individual scintillator pieces are chosen to match the HB tower geometry in η and ϕ. Scintillators, with a thickness of 10 mm, line the outside of the outer vacuum tank of the coil covering the region given by $-1.2 < \eta < 1.2$. The HO scintillators sample the energy in penetrating hadronic showers leaking out the back side of the calorimeters and so serve as a tail-catcher beyond the magnet coil. The system is divided into 5 sections along η, referred to as Rings $-2, -1, 0, 1$, and 2. The fixed Ring 0 has two scintillator layers on either side of an iron absorber with a thickness of about 18 cm, at radial distances of 3.850 m and 4.097 m respectively. The other rings have single layers at a radial distance of 4.097 m. Each ring covers 2.5 m in z.

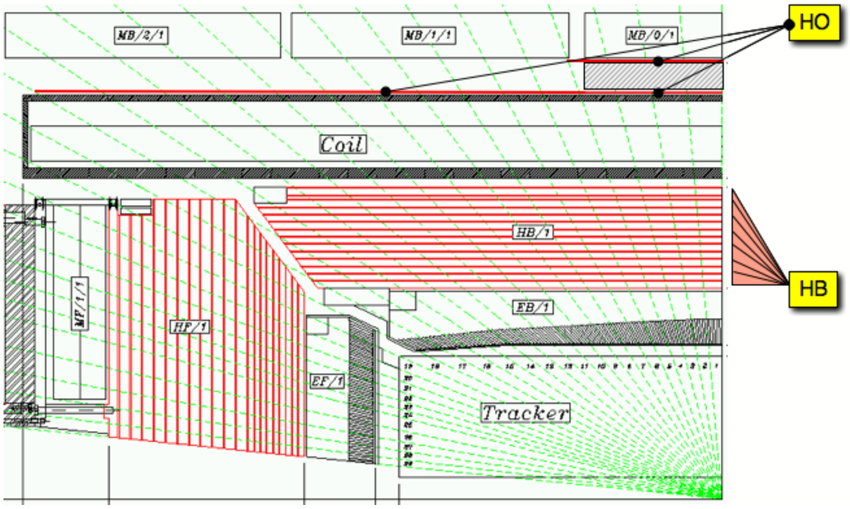

Figure 2: Layout of the CMS calorimeters

3 Algorithm

The basic idea of the muon identification algorithm is to extrapolate each reconstructed silicon track outward to its most probable location within each detector system of interest (ECAL, HCAL, HO, muon system). The track extrapolation takes into account the magnetic field and energy loss via the GEANE software package [7]. The algorithm then searches in a cone around that most probable location for any signals that might be associated with the track of interest. The cone sizes used for making these searches are different for each detector system and are parameterized as functions of the p_{T} and η of the silicon track. Optimization of cone sizes is based on studies of simulated event samples. After collecting the associated signals from each detector system, the algorithm determines a combined compatibility value corresponding to how well the observed signals fit with the hypothesis that the silicon track used to seed the algorithm is produced by a muon. The assignment of the compatibility value is somewhat arbitrary and based primarily on studies of various simulated event samples. The compatibility variable output by the algorithm is constructed so that different physics analyses can make different cuts on the minimum value required to identify muons. In choosing this threshold, each analysis can independently optimize the trade off between muon selection efficiency and the background fake rate for muons.

3.1 Calorimeter Identification

The minimum-ionizing signature of muons in the calorimeter can be used to help identify reconstructed tracks produced by muons. The identification algorithm looks for energy deposits associated with candidate tracks in both the electromagnetic and hadronic sections of the calorimeter and compares the observed energies with those expected for a minimum-ionizing particle. In the barrel region of the detector ($|\eta| < 1.2$), the algorithm also checks to see if a signal is observed in the additional outer hadronic calorimeter (HO), a scintillator layer located just outside of the superconducting solenoid in front of the inner muon chambers. Particles that enter this layer, having passed through the material in the calorimeter modules and magnet, are more likely to be minimum ionizing. In addition, any excess energy deposition in cells from sources such as pileup events should have less of an effect in the outer layers. There should, therefore, be a relatively lower probability of misidentification in the outer layers of the calorimeters, especially in the HO.

The muon identification algorithm extrapolates the seed track to its most likely location within each calorimeter volume. In the case of the HO layer, the location of the extrapolated track at the innermost muon chambers is used. The algorithm determines the total energy associated with the track candidate by summing the energies in towers whose centers are within some $\Delta R = \sqrt{(\Delta\eta)^2 + (\Delta\phi)^2}$ of the extrapolated track position. The value of ΔR is optimized separately for each calorimeter system to account for differences in tower granularities and to ensure that a big enough search cone is used to collect all of the energy associated with muons that either share their energy in adjacent cells or undergo significant multiple scattering. Optimization of cone sizes is also done independently for three separate bins in track η: barrel ($|\eta| < 0.8$), overlap ($0.8 < |\eta| < 1.2$), and endcap ($1.2 < |\eta|$) to account for differences in the calorimeter modules used in these regions. In order to avoid collecting energies not directly associated with the candidate track, the ΔR values used by the algorithm in each region are chosen to be as small as possible. However, they are not so small that a high collection efficiency for the energies associated with real muon tracks is not maintained. For the finely segmented electromagnetic calorimeter modules, studies of simulated single-muon event samples advocate optimal ΔR values between 0.02 and 0.03 (all energy deposited in one crystal). In the case of the more coarsely segmented hadronic calorimeter modules and the HO scintillator layer, bigger ΔR values between 0.08 and 0.13 are found to be the optimal choice.

The energy thresholds for observing the minimum-ionizing calorimeter signals are also important. For the offline algorithm, we typically attempt to make the single-tower thresholds as low as possible so that we can observe the small minimum-ionizing signal, especially in the case of the signals from the electromagnetic calorimeter. The minimum-ionizing energy expected to be deposited in the crystals is on the order of 300 MeV in the barrel region and 400 MeV in the endcap. Due to the fact that a high threshold on the order of 500 MeV is applied during the online readout of the endcap crystals, it is not always possible to observe the minimum-ionizing signal in the forward-electromagnetic calorimeter modules. A much lower threshold of about 60 MeV is applied during the online readout of the barrel crystals, which means that there is a much higher efficiency for observing the minimum-ionizing signal in the central electromagnetic calorimeter modules. The difference is illustrated in Fig. 3. The top and bottom figures show the electromagnetic energy returned from the muon identification algorithm for single $p_{\mathrm{T}} = 10\ \mathrm{GeV}/c$ muon tracks in the barrel and endcap regions of the detector. Note that in the endcap region, there are a substantial number of cases where the algorithm finds no electromagnetic energy associated with the track. For the hadronic calorimeter modules, the online readout thresholds are well below the threshold of the expected minimum-ionizing signal. Therefore, we apply an offline single-tower threshold on the order of 700 MeV within the identification algorithm for forming the hadronic calorimeter energy sum. This threshold is applied to remove potentially noisy towers.

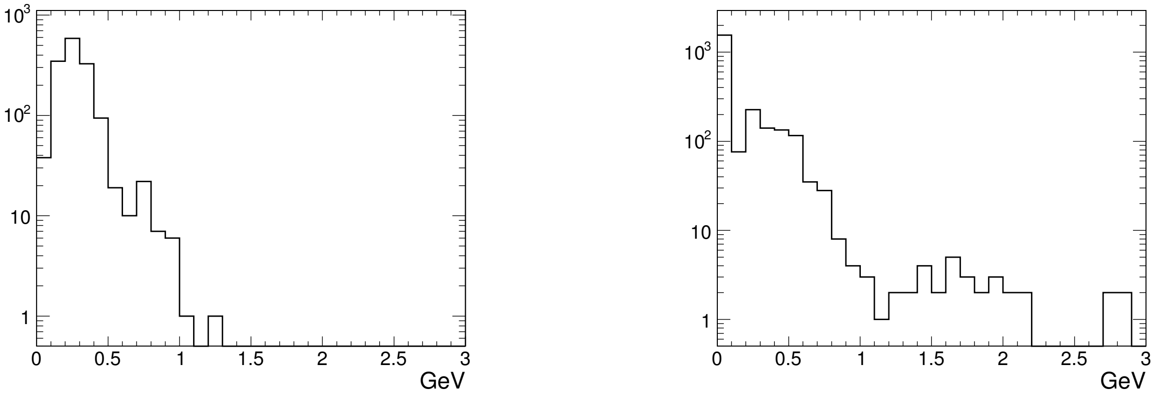

Figure 3: Electromagnetic calorimeter energy associated with single $p_{\mathrm{T}} = 10\ \mathrm{GeV}/c$ muon tracks as returned by the muon identification algorithm for the barrel (left) and endcap (right) regions of the detector. The significant number of zeroes returned for muons in the endcap region is due to the high online thresholds applied in the readout of the endcap crystals.

Based on the measured energies associated with candidate tracks, the muon identification algorithm calculates a compatibility value between zero and one that attempts to describe how consistent these energies are with respect to what one expects for a muon. The compatibility value is obtained from a three-dimensional likelihood function of the form

$$\frac{P_S(x) \cdot P_S(y) \cdot P_S(z)}{P_S(x) \cdot P_S(y) \cdot P_S(z) + P_B(x) \cdot P_B(y) \cdot P_B(z)} \,, \tag{1}$$

where P_S and P_B are the signal and background probabilities as functions of the measured energies in the electromagnetic calorimeter (x), the hadronic calorimeter (y), and the HO scintillator layer (z). The signal and background probability distributions are obtained from simulated samples of single-muons and pions, respectively. Independent distributions are obtained for the barrel, overlap, and endcap regions of the detector and for different track p_{T} ranges. Figure 4 shows example $P_S(x)$ and $P_B(x)$ functions obtained from simulated single $p_{\mathrm{T}} = 10\ \mathrm{GeV}/c$ muon and pion events for both the barrel and endcap regions based on the associated ECAL energy deposits measured by the muon identification algorithm. The corresponding $P_S(y)$ and $P_B(y)$ functions obtained from the same single particle samples and based on the associated HCAL energy deposits found by the algorithm are shown in Fig. 5. Because there is no HO scintillator layer in the endcap region of the detector, the $P_S(z)$ and $P_B(z)$ functions for this region are set to one. The resulting compatibility values for tracks associated with simulated $p_{\mathrm{T}} = 10\ \mathrm{GeV}/c$ single muons and pions are shown in Fig. 6 for both the barrel and endcap regions of the detector.

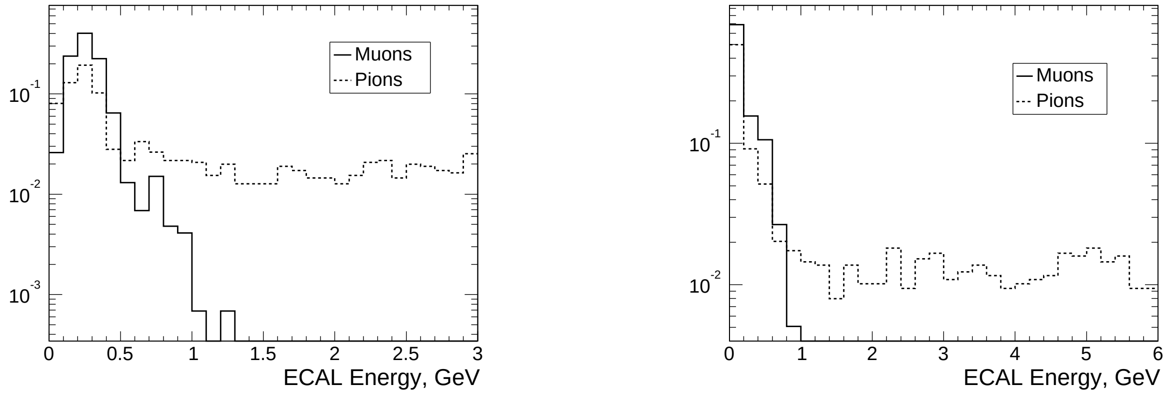

Figure 4: Example $P_S(x)$ and $P_B(x)$ functions obtained from simulated single $p_{\mathrm{T}} = 10\ \mathrm{GeV}/c$ muon (solid lines) and pion (dashed lines) events in the barrel (left) and endcap (right) regions of the detector based on associated energy deposits in the ECAL measured by the muon identification algorithm.

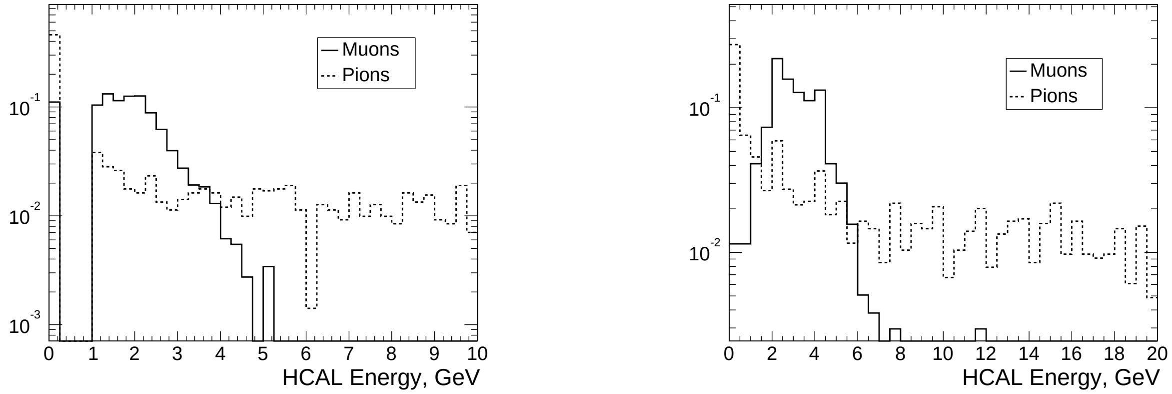

Figure 5: Example $P_S(y)$ and $P_B(y)$ functions obtained from simulated single $p_{\mathrm{T}} = 10\ \mathrm{GeV}/c$ muon (solid lines) and pion (dashed lines) events in the barrel (left) and endcap (right) regions of the detector based on associated energy deposits in the HCAL measured by the muon identification algorithm.

3.2 Muon Detector Identification

Reconstructed hit information from the muon detectors can be used to identify muon candidates even in cases where the stand-alone muon reconstruction fails. Low-p_{T} muons, in particular, can be bent back in the magnetic return field toward the interaction region or range out in the magnet yoke. In these cases, no hits are produced in the outermost layers of the muon detectors, and consequently stand-alone reconstruction is less efficient. Conversely, muon detector hits coming from even a single inner layer that can be associated with a reconstructed silicon track are potentially helpful in determining the muon compatibility of that track.

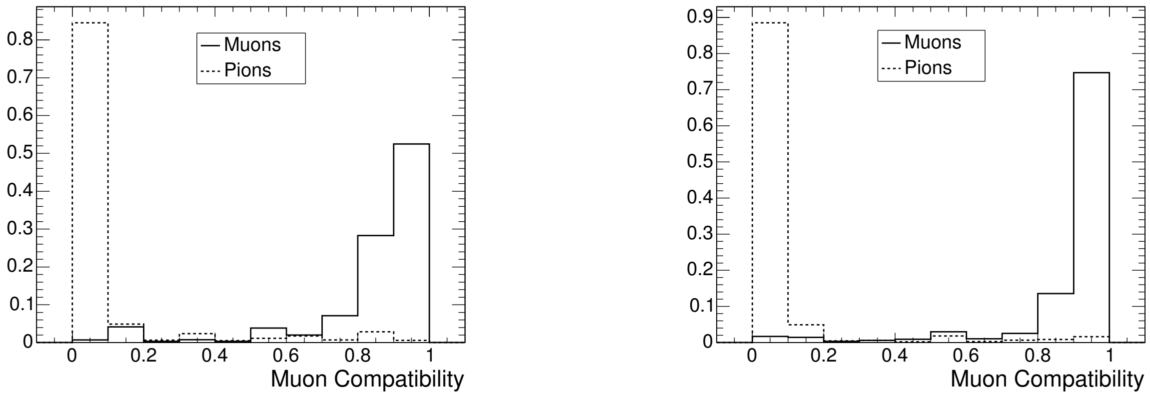

Figure 6: Muon compatibility values for silicon tracks associated with simulated $p_{\mathrm{T}} = 10\ \mathrm{GeV}/c$ single muons (solid lines) and pions (dashed lines) in the barrel (left) and endcap (right) regions of the detector. The compatibility values shown here are based solely on observed energy deposits in the calorimeter matched with the candidate track.

To incorporate muon detector hit information into the muon identification algorithm, silicon tracks are extrapolated sequentially into each layer of the muon detector. A search road is defined to look for hits and reconstructed segments within the layer that may be compatible with the extrapolated trajectory. For each potential matching hit or segment, the algorithm calculates a χ^2 measuring the compatibility of the position and direction (for segments) with those of the extrapolated track at the corresponding muon detector layer. The algorithm defines hits and segments to be associated with the silicon track if the corresponding χ^2 is below a programmable threshold. Using this definition, the algorithm outputs a list of matching hits and segments for each reconstructed track.

Using this list, the identification algorithm calculates a second muon compatibility value for each track based solely on muon detector hit information. The weight assigned to a single matching segment or hit depends on the dimensional content. Drift tube hits, for example, provide matching information in only one dimension. Drift tube chamber segments, on the other hand, contain matching information in two or even four dimensions if hits from all superlayers are incorporated. CSC and RPC hits provide slightly better matching in two dimensions, while CSC segments also provide ideal matching in all four dimensions. Matching hits and segments are also weighted by layer. Outer-layer hits and segments are more likely to be associated with a real muon since more material must be traversed to reach these layers, while inner-layer hits are more likely to be associated with punch-through of hadronic particles.

For each silicon track, the algorithm assigns a compatibility value between zero and one based on the number of matching muon detector segments and hits. The calculation is designed so that tracks matching to the best possible combination of hits and/or segments in each of the muon detector layers have a corresponding compatibility value of one. Of course, based on this definition, silicon tracks with an associated compatibility value near one are almost sure to be globally reconstructed as muons. In the case of muon identification, therefore, cuts on the compatibility value designed to recover muon reconstruction inefficiencies will need to be set well below this maximum value.

As discussed previously, the algorithm weights each piece of matching hit information based on the particular layer of the muon detector that it comes from. Hit information in the Drift Tube (DT) Chambers and Cathode Strip Chambers (CSC) makes up 70 % of the total compatibility value. The remaining 30 % is based on matching hit information in the Resistive Plate Chambers (RPC). Within the DT and CSC systems, hit information is further weighted by detector layer. Starting with the inner layers, matching hit information from each of the four detector layers makes up 10 %, 15 %, 20 %, and 25 % (70 % total) of the total compatibility value. Matching RPC hits are also weighted by detector layer. There are six RPC layers in the barrel contributing 2 %, 4 %, 4 %, 6 %, 6 %, and 8 % (30 % total) from inner to outer layer to the total compatibility value. Similarly, there are four RPC layers in the endcap that contribute 5 %, 5 %, 8 %, and 12 % (30 % total) from inner to outer. In order for a DT or CSC layer to contribute its full assigned weight to the compatibility value, a matching four-dimensional segment must be found on that particular layer. In the case where the only matching segments found on a particular DT layer are two-dimensional, the layer contributes only half of its maximum weight to the compatibility value. Finally, if no matching segments are found on a given DT or CSC layer, the algorithm counts up the number of matching hits on that layer (up to a maximum of twelve hits for DT layers and six hits for CSC layers). If the maximum number of matched hits is found, the layer still contributes half of its maximum weight to the compatibility value. If less than the maximum number of matching hits are found, the contribution from the layer is further reduced by the ratio of the observed number of matching hits to the maximum number. In the case of RPC layers, only one matched hit is required for the layer to contribute its maximum weight to the compatibility value.

Based on the algorithm described above, the muon compatibility value distributions for tracks associated with simulated $p_{\mathrm{T}} = 10\ \mathrm{GeV}/c$ single muons and pions are shown in Fig. 7 for the barrel and endcap regions of the detector.

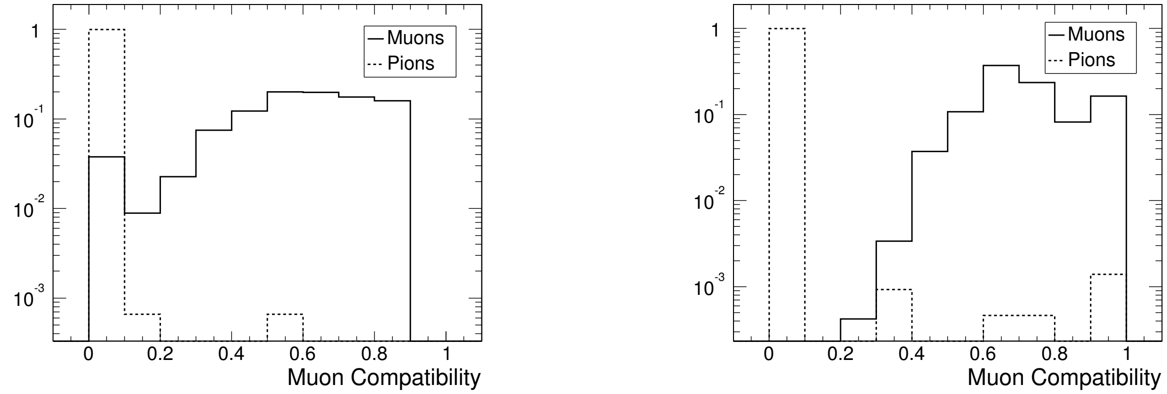

Figure 7: Muon compatibility values for silicon tracks associated with simulated $p_{\mathrm{T}} = 10\ \mathrm{GeV}/c$ single muons (solid lines) and pions (dashed lines) in the barrel (left) and endcap (right) regions of the detector. The compatibility values shown here are based solely on matched hits and segments in the muon detectors.

4 Software Design

The software has been implemented in C++ using object-oriented programming techniques and is part (package `MuonReco/MuonIdentification`) of the official CMS reconstruction package ORCA [1].

Identification algorithms are grouped into two classes (`MuonIDByMuonSystem` and `MuonIDByCalorimetry`) based on the component of the detector used for the identification. Each algorithm class inherits from a common base class (`MuonIDBaseAlgorithm`) and outputs its results as an object of the `MuonIDResult` class. Objects of this class, in addition to providing a tag that identifies particles as muons and the associated compatibility value used in determining the tag, also provides access to all the information used in the identification, whether that be hits and segments in the muon chambers, locally reconstructed tracks, calorimeter energy, or other relevant pieces of detector information. The only input that is required for muon identification is the reconstructed track of the particle from the tracker. In addition, a class `MuonIdentification` has been implemented that conducts muon identification using both available algorithms. The user can choose either to use the individual algorithms or the combined algorithm. A typical piece of user code will look like the following:

```
RecTrack t;
MuonIdentification mid;
MuonIDResult r = mid(t);
cout << r. probability() << endl;
```

or

```
RecTrack t;
MuonIDByMuonSystem mid1;
MuonIDResult r1 = mid1(t);

MuonIDByCalorimetry mid2;
MuonIDResult r2 = mid2(t);
cout << r1. probability() << " " << r2. probability() << endl;
```

In addition to the implementation of the identification algorithms, a test program is provided with the package (`MuonReco/MuonIdentification/test/MuonIdentificationTest.cpp`).

5 Performance

The performance of the muon identification algorithm was studied on several simulated event samples. For these studies, a silicon track is considered to be identified as a muon if its associated compatibility value based on energy deposits in the calorimeter is above 0.8 and its associated compatibility value based on hit and segment information in the muon detectors is greater than 0.4. These cut values are programmable and in general require optimization for specific algorithm applications. Here, the same cut values are used on several different types of event samples to provide a baseline overview of algorithm performance. Low-p_{T} muons are of particular interest since in a significant fraction of cases these muons do not produce hits in the outer muon detector layers and are therefore more difficult to reconstruct using the standard stand-alone algorithm. The algorithm was run on a sample of 50,000 simulated single-muon events. The muons were generated flat in ϕ and η (from -2.5 to 2.5) with a single-p_{T} value of $5\ \mathrm{GeV}/c$. The single muons were generated on top of simulated pile-up events corresponding to a luminosity of 2×10^{33} cm^{-2} s^{-1}. The efficiency distributions for both global muon reconstruction and global muon reconstruction plus muon identification are shown on the left-hand side of Fig. 8, as a function of the simulated muon pseudorapidity. For the events in this sample, the efficiency for reconstructing single, low-p_{T} muons is 68.7%. Adding muon identification as an additional selection mechanism increases the overall selection efficiency for the muons in this sample by roughly 15% (for a combined efficiency of 78.6%). The muon identification algorithm was also run on all of the non-muon tracks in these events to investigate the rate at which the algorithm mis-identified these tracks as muon candidates. The fake rate as a function of track η is shown in the distribution on the right-hand side of Fig. 8. Only 30 out of over 250,000 non-muon tracks in these events are identified as muon candidates by the algorithm.

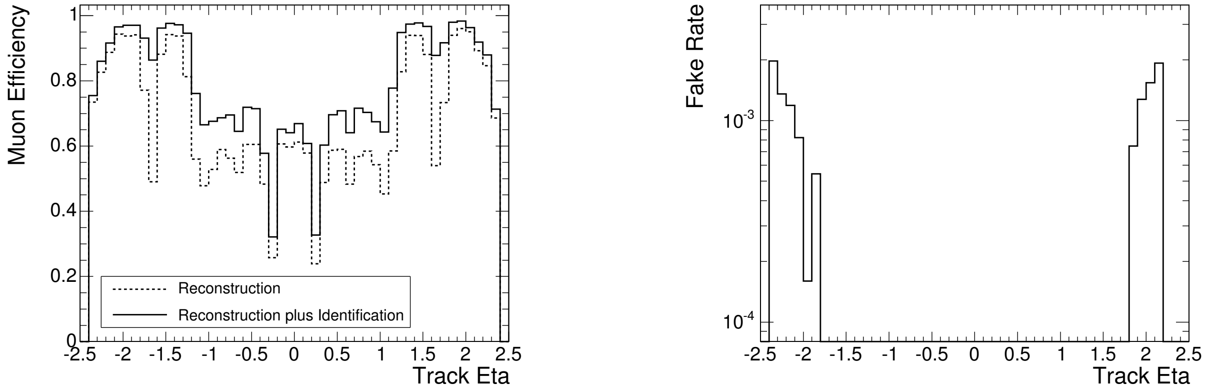

Figure 8: Efficiencies for global muon reconstruction (dashed lines) and global muon reconstruction plus muon identification (solid lines), as a function of pseudorapidity for $p_T = 5\ \mathrm{GeV}/c$ single muons (left). Fake rate at which non-muon tracks in the same events are tagged as muon candidates using the muon identification algorithm also as a function of pseudorapidity (right). The observation of fake rates equal to zero in the central part of the detector ($|\eta| < 1.8$) is due to insufficient statistics.

The muon identification algorithm was also run on a sample of simulated $H \rightarrow WW \rightarrow \mu\mu\nu\nu$ events generated using a Higgs mass of 200 GeV/c^2. The events include minimum-bias pile-up corresponding to a luminosity of 2×10^{33} cm^{-2} s^{-1}. Due to the low overall production cross section for this process, observing a signal in the data requires maintaining high event selection efficiency. Since the transverse momentum of the lower-p_{T} muon is observed to be less than $10\ \mathrm{GeV}/c$ in roughly 20 $\%$ of these events, muon identification can potentially be a useful tool for increasing the overall selection efficiency in this channel. Because the algorithm has not yet been optimized for selecting very low-p_{T} muons, we restrict this study to the subset of events where the p_{T} of both muon candidates is greater than $5\ \mathrm{GeV}/c$. The distributions on the right-hand side of Fig. 9 show the selection efficiency for events in this channel as a function of the simulated p_{T} of the lower-p_{T} muon, using both global reconstruction and global reconstruction plus muon identification. From these distributions, we observe a net gain on the order of 5 $\%$ in the overall selection efficiency incorporating the muon identification algorithm. The rate at which non-muon tracks in these events are tagged as muons by the identification algorithm was also measured. The fake rate as a function of track p_{T} is shown on the right-hand side of Fig. 9. Out of over 750,000 non-muon tracks in these events, less than 125 are identified as muon candidates using the algorithm.

Low-p_{T} muons are also produced in the semi-leptonic decays of heavy quarks. The tagging of muons within jets (soft-lepton tagging) is therefore a useful tool in selecting jets originating from bottom quark decays (an important

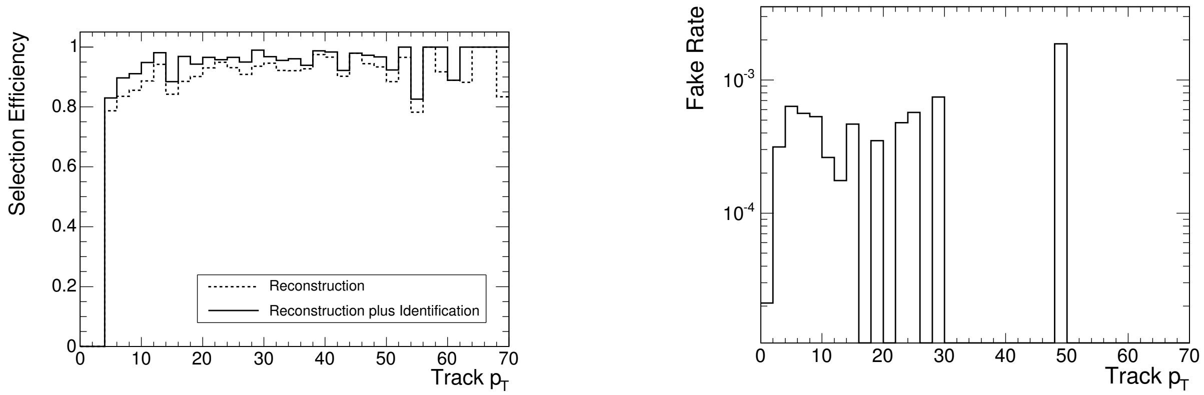

Figure 9: $H \rightarrow WW \rightarrow \mu\mu\nu\nu$ event selection efficiencies using global muon reconstruction (dashed lines) and global muon reconstruction plus muon identification (solid lines), as a function of the p_{T} of the lower-p_{T} muon in the events (left). Fake rate at which non-muon tracks in the same events are tagged as muon candidates using the muon identification algorithm as a function of track p_{T} (right). The observation of fake rates equal to zero for the majority of p_{T} values above 15 GeV/c is due to insufficient statistics.

requirement for many analyses). In order to see if the muon identification tool might be useful in improving the efficiency for soft-lepton tagging in bottom quark jets, the algorithm was run on a simulated sample of bottom quark jets with generated p_{T} values between 50 and 80 GeV/c^2. The events were generated on top of simulated pile-up events corresponding to a luminosity of 2×10^{33} cm^{-2} s^{-1}. The p_{T} spectrum of the muons contained within this sample of bottom quark jets is shown on the left-hand side of Fig. 10. Because the muon identification algorithm has not yet been optimized for selecting very low-p_{T} muons, our soft lepton tagging measurements are made using the subset of muons in this sample with p_{T} values greater than 5 GeV/c. The pseudorapidity distribution of the muons within bottom quark jets that satisfy this minimum p_{T} requirement is shown on the right-hand side of Fig. 10.

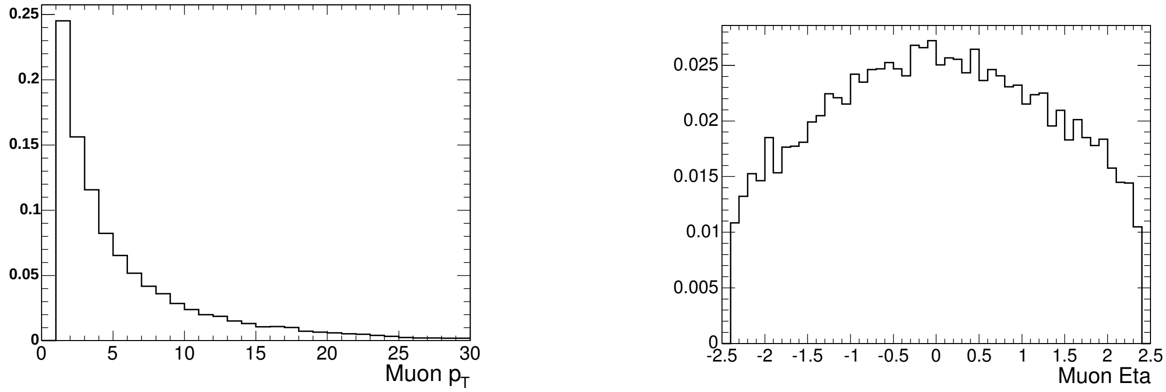

Figure 10: Transverse momentum spectrum (left) of muons contained within our simulated sample of bottom quark jets and the pseudorapidity distribution (right) for those muons within the sample with p_{T} values greater than 5 GeV/c.

The distributions shown in Fig. 11 are efficiency curves for both global muon reconstruction and global muon reconstruction plus muon identification for the muons produced in the semi-leptonic decays of the bottom quarks in these events, as functions of the simulated muon p_{T} and pseudorapidity. The global reconstruction efficiency for these muons is 71% and incorporating the muon identification algorithm increases the overall selection efficiency to 84%. Because the matching of stand-alone tracks in the muon detectors with tracks in the silicon tracker is a requirement of global muon reconstruction and more difficult within the noisy environment of bottom quark jets, the effect of including stand-alone tracks in our soft lepton tagging definition was also studied. Here, muons within bottom quark jets are also considered to be reconstructed if a stand-alone track in the muon detectors is found within ($\Delta R = \sqrt{(\Delta\eta)^2 + (\Delta\phi)^2} < 0.025$) of the simulated muon trajectory. The resulting efficiency curves for global or stand-alone reconstruction and global or stand-alone reconstruction plus muon identification are shown in Fig. 12. Using this definition, the selection efficiency for soft leptons within bottom quark jets based on reconstruction is

83% and incorporating the muon identification algorithm increases the overall selection efficiency to 89%.

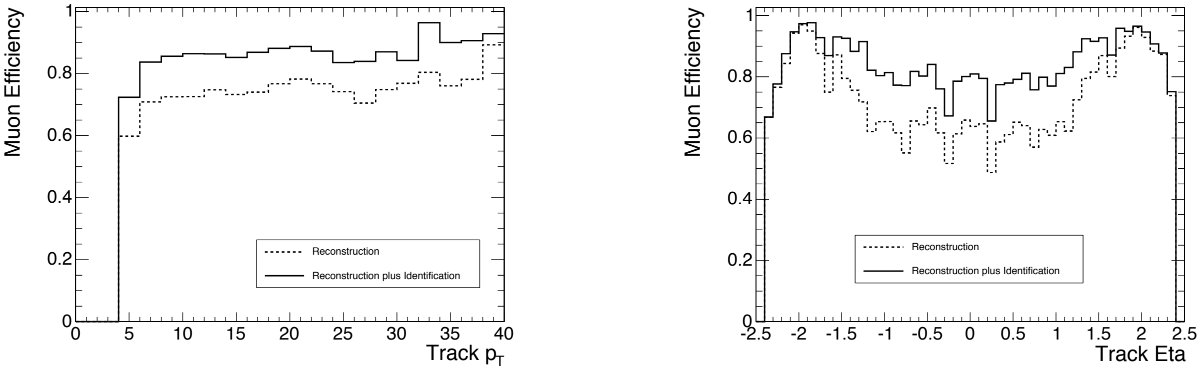

Figure 11: Efficiencies for global muon reconstruction (dashed lines) and global muon reconstruction plus muon identification (solid lines) for prompt muons contained within bottom quark jets, as a function of muon p_{T} (left) and pseudorapidity (right).

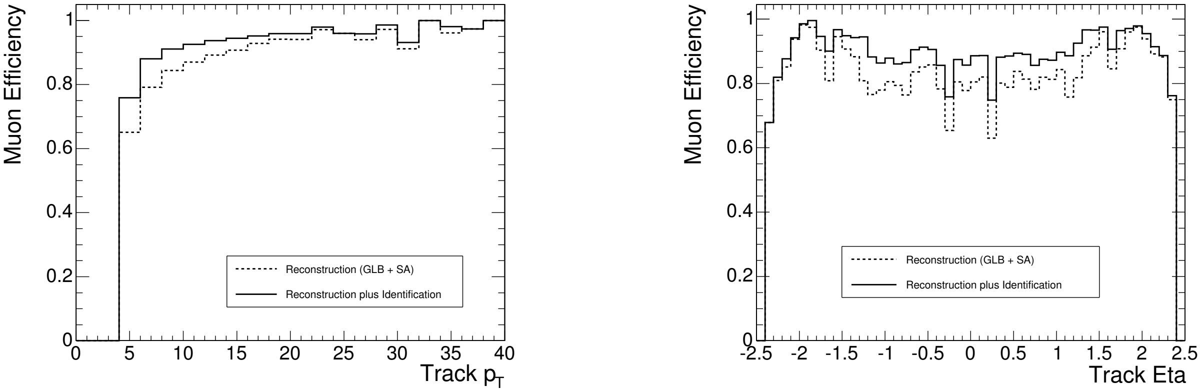

Figure 12: Efficiencies for global plus stand-alone muon reconstruction (dashed lines) and global plus stand-alone muon reconstruction plus muon identification (solid lines) for prompt muons contained within bottom quark jets, as a function of muon p_{T} (left) and pseudorapidity (right).

To be useful in soft-lepton tagging, the associated fake rate of the algorithm (the rate at which non-muon tracks within jets are identified as muons) must also be low since jets originating from both light and heavy quarks, as well as those from gluons, contain many non-muon tracks. The algorithm fake rate is studied using reconstructed pion and kaon tracks found within the subset of bottom quark jets from our simulated sample that are found to contain no prompt muons. The efficiencies for tagging these tracks as muons using global muon reconstruction and global muon reconstruction plus muon identification are shown in Fig. 13 for pions and in Fig. 14 for kaons as functions of the simulated track p_{T} and pseudorapidity. The measured fake rate at which tracks within bottom quark jets are globally reconstructed as muons is 0.17% for pions and 0.33% for kaons. Adding muon identification as an additional selection tool, increases the muon fake rates per track to roughly 0.20% for pions and 0.38% for kaons. The small increases in the observed fake rates indicate that the muon identification algorithm can be potentially useful in soft lepton bottom quark tagging. Figure 15 shows distributions for the number of tracks, pion tracks, and kaon tracks with $p_{\mathrm{T}} > 5\ \mathrm{GeV}/c$ per bottom quark jet for those jets within our simulated sample observed to contain no prompt muons. Note that these distributions are for all bottom quark jets without prompt muons in our simulated sample, irrespective of whether the jets are reconstructible in any offline algorithm. Based on these distributions and the fake rate estimates for pion and kaon tracks quoted above, it is possible to extract a rough estimate for the fake rate per jet. However, we note that this approach will result in an over-estimate of the fake rate since it ignores potential correlations between tracks contained within individual jets.

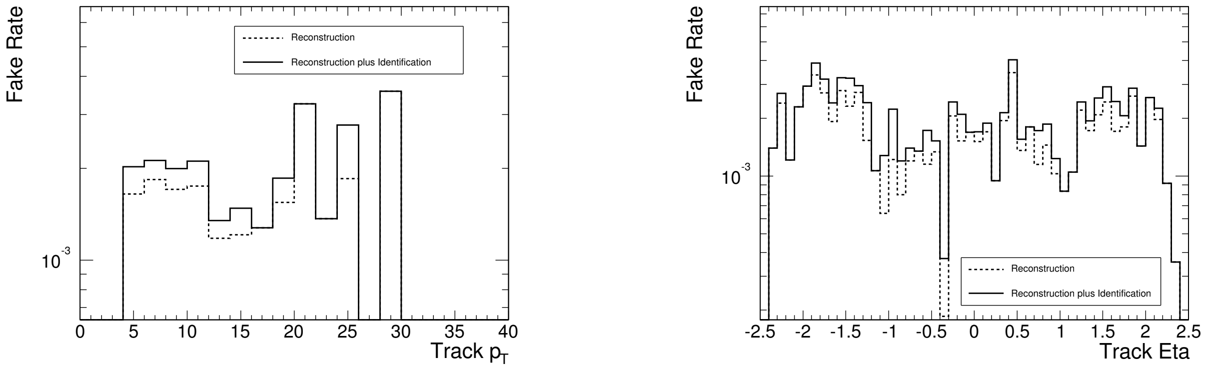

Figure 13: Fake rates for global muon reconstruction (dashed lines) and global muon reconstruction plus muon identification (solid lines) for pions contained within bottom quark jets, as a function of simulated pion track p_{T} (left) and pseudorapidity (right).

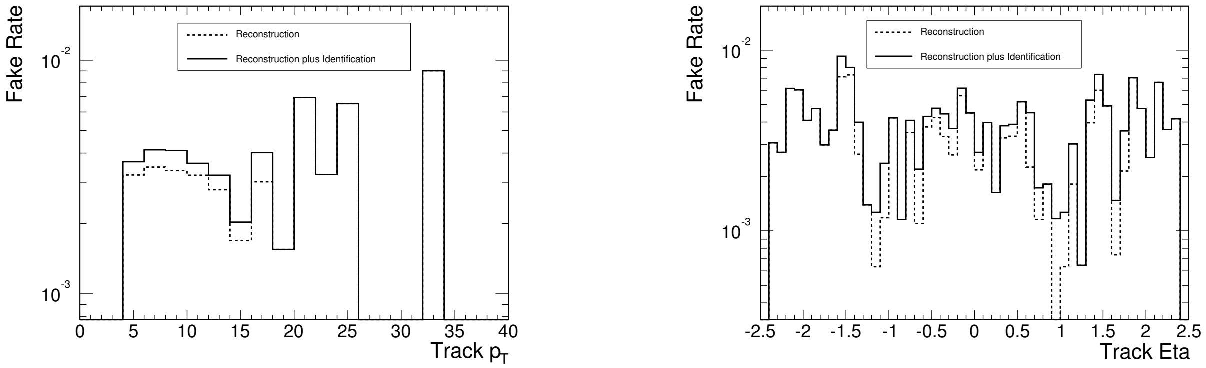

Figure 14: Fake rates for global muon reconstruction (dashed lines) and global muon reconstruction plus muon identification (solid lines) for kaons contained within bottom quark jets, as a function of simulated kaon track p_{T} (left) and pseudorapidity (right).

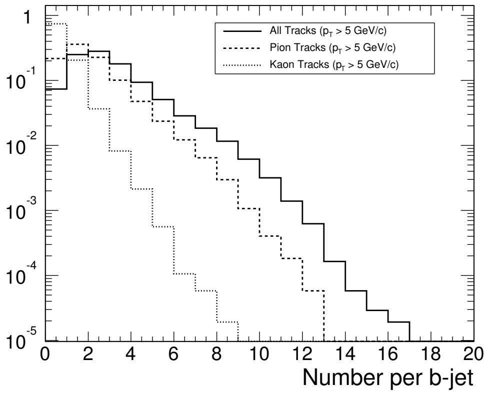

Figure 15: Number of tracks (solid line), pion tracks (dashed line) and kaon tracks (dotted line) with $p_{\mathrm{T}} > 5\ \mathrm{GeV}/c$ per bottom quark jet for the jets in our simulated sample containing no prompt muons.

6 Summary

This note describes an initial implementation of a muon identification algorithm to aid in the offline selection of muon candidates in events to be collected with the CMS detector. The algorithm is designed to complement the standard muon track reconstruction algorithm which starts by reconstructing stand-alone tracks in the muon detectors and then attempts to match these with tracks reconstructed in the silicon detector. As described in the note, the muon identification algorithm starts with all reconstructed tracks from the silicon detector and assigns a compatibility value for each that quantifies how well the tracks fit with a muon hypothesis based on matching hit information from the calorimeters and muon systems. We expect the muon identification tool to be useful for many physics analyses, particularly those that involve selection of low momentum muon candidates. In general, the algorithm will need to be tuned for each specific application to obtain optimal performance. The studies presented in this note are not intended to describe the ultimate performance of the algorithm in its potential applications, but rather to give a general overview of the untuned algorithm's performance in selecting muons associated with different physics signatures.

References

[1] CMS Collaboration *ORCA:CMS Reconstruction Package*, Site located at http://cmsdoc.cern.ch/orca.

[2] CMS Collaboration, *The Muon Project, Technical Design Report*, CERN/LHCC 97–32 (1997).

[3] S.Lacaprara, *The CMS Muon System: Physics Performance*, EPJDirect A1, 1-11 (2003).

[4] CMS Collaboration, *The Tracker Project, Technical Design Report*, CERN/LHCC 98–06 (1998).

[5] CMS Collaboration, *ECAL Technical Design Report*, CERN/LHCC 97-33, CMS TDR 4 (1997).

[6] CMS Collaboration, *HCAL Technical Design Report*, CERN/LHCC 97-31, CMS TDR 2 (1997).

[7] V. Innocente, M. Maire and E. Nagy, “GEANE: Average Tracking and Error Propagation Package”, CERN Program Library, IT-ASD W5013-E (1991).